Progress in Additive Manufacturing (2025) 10:11683–11695
https://doi.org/10.1007/s40964-025-01309-9

RESEARCH

Thermal modeling and experimental validation of dot-by-dot wire arc additive manufacturing

Masoud Abbaszadeh[1] · **Gustavo H. S. F. L. Carvalho**[1] · **Gianni Campatelli**[1] · **Niccolò Grossi**[1]

Received: 14 May 2025 / Accepted: 16 August 2025 / Published online: 23 August 2025

Abstract

This study investigates Dot-by-Dot Wire Arc Additive Manufacturing (DBD-WAAM), a novel variant of conventional Wire Arc Additive Manufacturing, which facilitates the fabrication of unconventional lattice structures. The research employs a combined approach of finite element method (FEM) simulations and experimental validation. FEM was utilized to simulate the DBD-WAAM process, analyzing the impact of key parameters such as idle time and heat input on interpass temperature. The simulation results were validated against experimental data. The heat-affected zone (HAZ) boundaries were identified through optical microscopy and compared with FEM predictions. Furthermore, the simulated temperature distribution was correlated with thermal imaging data recorded during the manufacturing process. Three distinct heat source models–semi-spherical, linearly decaying, and exponentially decaying–were employed to characterize the spatial distribution of heat input. The semi-spherical heat source model demonstrated superior predictive accuracy for both the heat-affected zone boundary and the temporal evolution of temperature. The findings confirm that the FEM model accurately predicts both the temperature distribution and the HAZ boundaries for DBD-WAAM with a maximum average error of approximately 15% for interpass temperature and 20% for substrate temperature in the worst case scenario. Finally, the study proposes a design curve, providing crucial information for selecting appropriate interpass idle times to ensure optimal thermal control between individual dots, and consequently a better control of the geometry and mechanical properties.

Keywords Dot-by-dot WAAM · Idle time · Interpass temperature · Thermal cycle · Finite element simulation

1 Introduction

The development of additive manufacturing (AM) processes in recent years has profoundly transformed the manufacturing sector [1], representing today one of the most investigated topics in engineering. Its evolution and transformative influence have also begun to impact the architecture and construction industries in several aspects [2, 3]. This change is driven by the AM's ability to produce components with enhanced performance, greater customization, and unparalleled design freedom, enabling the creation of complex and optimized geometries. This is particularly important for the additive manufacturing of metallic materials, given that conventional manufacturing processes, despite their fundamental role in engineering, do not offer these distinct advantages.

In general, AM processes involve a trade-off between geometric freedom, construction precision, mechanical properties, and productivity, where improvements in one characteristic typically necessitate compromises in another. Among these processes, the Wire Arc Additive Manufacturing (WAAM) process is particularly recognized for its superior productivity and excellent mechanical properties, despite having limitations in terms of geometric complexity [4]. The WAAM process, also known as arc-based direct energy deposition (DED), is a type of DED variant that integrates conventional wire-based arc welding with numerical control to build up metallic objects layer by layer [5]. Recent advancements, particularly the development of non-conventional deposition techniques like the dot-by-dot technique,

✉ Niccolò Grossi
niccolo.grossi@unifi.it

Masoud Abbaszadeh
masoud.abbaszadehshakarab@unifi.it

Gustavo H. S. F. L. Carvalho
gustavo.carvalho@unifi.it

Gianni Campatelli
gianni.campatelli@unifi.it

[1] Department of Industrial Engineering, University of Florence, Florence, Italy, Via di Santa Marta, 3, 50139

have progressively mitigated its inherent geometric fabrication limitations.

Dot-by-dot Wire Arc Additive Manufacturing (DBD-WAAM) [6], also known as Point-by-point [7], Skeleton Arc Additive Manufacturing (SAAM) [8] or as Interrupted metal deposition (IMD) [9], is a unique metal additive manufacturing process that enables a more precise deposition to produce structural parts with geometric complexity [10–12]. A similar technique is the CMT Cycle Step technology that can also be used for bead depositions [13, 14]. In contrast to the continuous bead deposition of conventional WAAM, DBD-WAAM operates by depositing successive, discrete drops (or "dots") of molten metal, enabling component fabrication through precisely placed individual droplets [15]. This technique allows for a more refined control over the deposition, and the building of vertical lattice structures and topologically optimized structures that would not be possible with conventional WAAM [8, 16]. Among its advantages, these structures are particularly well suited for on-site fabrication and customized architectural applications that require structural complexity, and material efficiency [6, 17, 18].

Nevertheless, this technique presents some limitations. A primary concern is the limited understanding of how process parameters affect DBD-WAAM, which are different from conventional WAAM due to its short and intermittent deposition nature. Furthermore, the productivity is significantly lower than conventional WAAM, not only due to the inherently slower deposition but also because of insufficient knowledge regarding optimization of the idle time (dwell time) between dots. For example, a minor adjustment of the idle time from 2 s to 5 or 1 s can profoundly impact the total manufacturing time. However, the optimal selection of this idle time is not straightforward, often involving complex trade-offs related to heat dissipation, solidification, geometry and microstructure.

Recent research on DBD–WAAM has primarily focused on process parameter optimization, toolpath planning, mechanical properties, and the applications of DBD–WAAM components. Regarding process parameters, Abe and Sasahara [19] proposed a real-time process control method, while Heimig et al. [20] focused on trajectory optimization strategies. More recently, Mao et al. [21] studied the effect of arc waveforms on the overall process and properties. Concerning material properties, Muller et al. [18] and Silvestru et al. [7] evaluate the mechanical properties of DBD-WAAM manufactured rods, while Yigit Hergul [22] investigated the microstructure of the rods. In terms of design perspectives, Laghi et al. [23] and Yu et al. [11] explored how structural design parameters influence performance and geometry, as well as broader design approaches for lattice structures. Finally, regarding potential applications, Mechtcherine et al. [15] and Classen et al. [17] focused on the integration of the DBD-WAAM components with concrete structures, particularly relevant for the construction and architecture sectors.

While the available research provides fundamental knowledge, two critical aspects for the development of the technique remain underexplored: strategies/knowledge to improve productivity and DBD–WAAM numerical simulation using the finite element method (FEM). Notably, one of the most effective and efficient approaches to comprehend the complex interplay of idle time on temperature, thermal cycle, microstructure, and geometry is through FEM. FEM enables comprehensive simulation of the thermal and mechanical aspects of manufacturing, which facilitates the improvement of mechanical properties and overall quality of components through the optimization of parameters [24], including heat input [25], interpass temperature [26] and deposition strategy [27]. Additionally, FEM reduces the need for trial-and-error by simulating the process before physical manufacturing, saving valuable time and resources [28]. However, despite the extensive research on FEM-based simulations of conventional WAAM, research on modeling the DBD-WAAM process remains very incipient [29, 30]. In the numerical simulation of conventional WAAM, several heat source models are employed [30], and their applicability and accuracy for DBD-WAAM are not clear and require further investigation.

Therefore, this aims to develop a numerical model to simulate the DBD–WAAM, providing tools and knowledge to simulate and verify the impact of different deposition parameters, such as heat input and idle time, on the geometry and quality of the component. Several models of heat sources are employed to model the heat input distribution: semi-spherical, linearly, and exponentially decaying, to understand the best fit for DBD–WAAM. The accuracy of the developed FEM model was then validated against experimental data, including microstructural analysis to define the heat-affected zone (HAZ) boundaries, as well as the temperature distributions captured using a thermal camera. Furthermore, these simulations are intended to generate design curves to facilitate the selection and optimization of critical parameters, ultimately minimizing idle time and enhancing productivity, one of the main issues of DBD–WAAM.

2 Numerical methodology

The DBD–WAAM deposition was simulated using the FEM software ABAQUS/Standard, focusing exclusively on the overall power transferred to both the filler and base materials (i.e., the deposited and substrate materials). Hence, simplifying the simulation by omitting the need for complex numerical models of heat and mass transfer in the electric arc, as well as heat transfer resulting from fluid flow in the melt pool. For the simulation of the DBD–WAAM process within the finite element environment, the following initial pre-processing stages are considered to ensure effective program execution:

2.1 Geometry discretization

The first step in simulating the DBD WAAM process involves discretizing the geometry of the final metal part, achieved through the use of three-dimensional elements. During the pre-processing phase, both the substrate (base plate) and the deposited rods are discretized into elements, requiring the generation of all elements for each of these components. To accomplish this, rods were positioned at the center of the substrate and perfectly bonded to the substrate plate. The diameter and height of the rods correspond to the dimensions produced in the test series discussed in Sect. 3.1. To reduce computational costs, symmetry boundary conditions are applied in the symmetry plane, as commonly adopted in such type of simulation [30, 31], as shown in Fig. 1.

The model is discretized using 8-node convection/diffusion brick elements (DCC3D8). A fine mesh is applied to both the rod and the substrate, particularly near the junction area, where temperature rises rapidly due to the heat source during deposition. In the rod zone, a 1 mm mesh size was used for the substrate, adopting a mesh coarsening strategy for the rest of the plate, as shown in Fig. 1. For the deposited dot-by-dot rod, the number of elements along the build direction of each dot is consistently set to be two (Fig. 1), resulting in approximately 0.25 mm, 0.5 mm and 0.75 mm mesh size for A, B and C case study respectively (see Table 3). The "inactive element method" [32] is employed to model material deposition during the heat transfer analysis of the DBD WAAM process. In this approach, the elements representing the deposited regions are initially inactive and are gradually activated in alignment with the heat source center.

2.2 Heat source modeling

In finite element modeling of the WAAM process, the heat source model is crucial for accurately representing the energy distribution between the base and filler materials. While the Goldak heat source model [33] is widely used to simulate heat distribution in the conventional WAAM process, it assumes a moving heat source, which is not applicable in the DBD WAAM process. In DBD WAAM, the welding torch is stationary at each step, and the heat source remains fixed during the deposition of each dot. Therefore, in this study, three Gaussian heat source models were considered to simulate the heat energy distribution: semi-spherical [34], linearly [35], and exponentially decaying [36]. These models are summarized in Table 1, where β represents the heat energy absorptivity, P is the power of the stationary heat source, and a, b, and c are the heat source dimensions. It is important to note that these dimensions are calibrated for each test case through a trial-and-error process, as discussed in Section 3.2. Additionally, the heat sources were placed on the substrate's or previously deposited top surface.

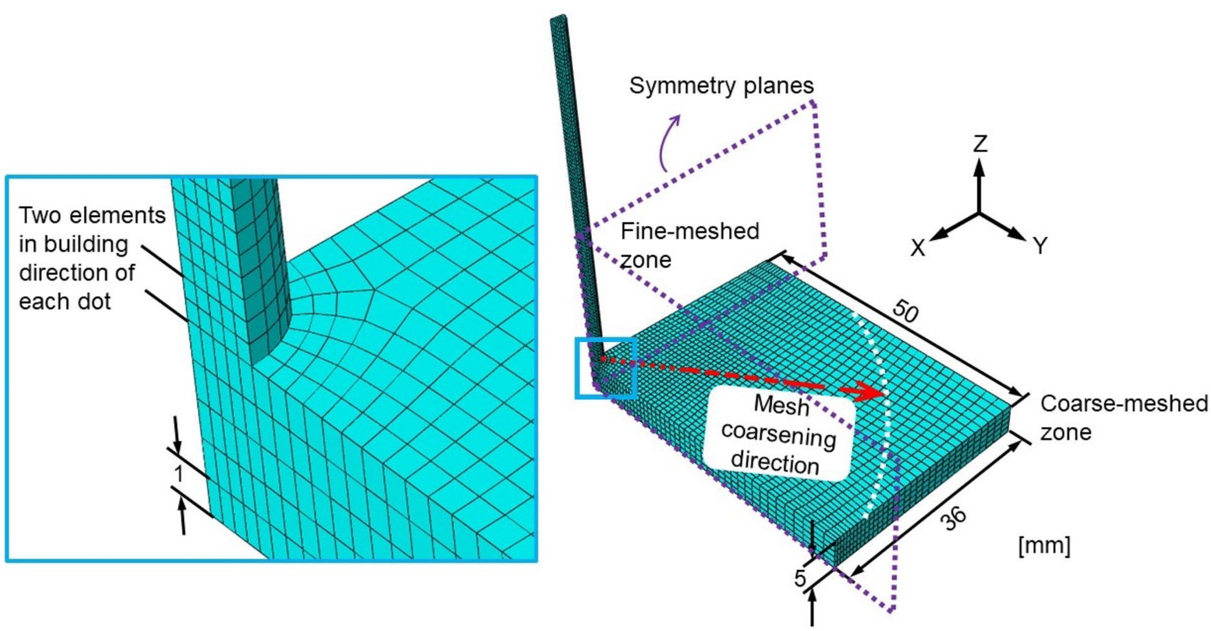

Fig. 1 Finite element model of the rod and substrate (dimensions in mm) using symmetry boundary conditions to reduce the model size. The mesh size was increased in the areas far from the heat source to optimize computational costs

Table 1 Mathematical representations of heat sources models used in this study

Heat source model	Mathematical equation
Semi-spherical [34]	$I(x,y,z) = \frac{2^{5/2}\beta.P}{\pi^{3/2}abc} exp[-2(\frac{x^2}{a^2} + \frac{y^2}{b^2} + \frac{z^2}{c^2})]$
Linearly decaying [35]	$I(x,y,z) = \frac{2P}{\pi.ab} exp[-2(\frac{x^2}{a^2} + \frac{y^2}{b^2})].f(z)$, $f(z) = \beta.\frac{2}{c}(1 - \frac{z}{c})$
Exponentially decaying [36]	$I(x,y,z) = \frac{2P}{\pi.ab} exp[-2(\frac{x^2}{a^2} + \frac{y^2}{b^2})].f(z)$, $f(z) = \beta.\frac{1}{c} exp[-\frac{z}{c}]$

2.3 Boundary conditions establishment

Free convection and radiation were applied to all surfaces of the base plate and the rods, as described by Eqs. 1 and 2. This helps to simulate the heat transfer from the material to the surrounding environment during the DBD WAAM process. In Eqs. 1 and 2, h is the convective heat transfer coefficient [$W/(m^2\,°C)$], ϵ is the emissivity, σ is the Stefan-Boltzmann constant and T_{surf} and T_{amb} are component's surface and ambient temperatures. The parameters used in Eqs. 1 and 2, which were implemented in this study, will be discussed in detail in section 3.2 in the context of the case study presented in this paper. To reduce the size of the finite element model and the overall CPU requirements, the conditions for symmetrical planes where the heat flux through these planes is zero were also taken into account [37].

$$q_c = -h(T_{surf} - T_{amb}) \quad (1)$$

$$q_r = -\epsilon\sigma(T^4_{surf} - T^4_{amb}) \quad (2)$$

3 Proposed model validation

While the numerical approach presented offers a general method for simulating the DBD WAAM process, this study specifically focuses on its application to low-carbon steel. The accuracy of the proposed model is verified by analyzing the correlation between the simulated and actual temperature distribution, as well as the boundary of the HAZ.

3.1 Experimental design and methodology

In this study, ER70S-6 filler wire with a diameter of 1mm was used to fabricate rods with varying diameters and lengths by depositing a series of dots on a mild steel substrate (S235JR) with dimensions of $100 \times 72 \times 5mm^3$ using the DBD WAAM method. The chemical compositions of the wire and substrate were provided by the manufacturers, and the nominal values are listed in Table 2.

A local shielding gas mixture consisting of 82% argon and 18% CO_2 was employed, with a constant flow rate of 15L/min. The deposition was performed using a Fronius TPS 320i GMAW power source, connected to a retrofitted 3-axis milling machine, as shown in Fig. 2a. The experimental setup for the CNC-based DBD WAAM process is illustrated in Fig. 2a. Figure 2b shows an example of a lattice structure produced DBD WAAM. Before deposition, the substrate was wire-brushed and cleaned with acetone to remove any organic contamination and prevent the formation of welding defects. It is important to note that the torch was held perpendicular to the substrate during the deposition process.

Table 3 provides an overview of the test series, detailing the process parameters employed, as well as the resulting rod diameters and average dot heights for each test. In this table, WFS denotes the nominal wire feed speed (noting that the actual wire feed speed is slightly lower), and arc-on time refers to the duration for which the arc remained active. DH and RD correspond to the average dot height and rod diameter, respectively. The contact tip to workpiece distance (CTWD) was initially set to 10mm and subsequently adjusted after each dot deposition based on the average dot height in the build-up direction. Furthermore, an interpass cooling time was applied after each deposition to mitigate excessive heat accumulation. The effect of this cooling time on the peak interpass temperature was also investigated.

During the deposition, a thermal camera (Optris PI640i) was used to measure temperatures, and the welding machine's start and stop signals were synchronized to ensure accurate data collection (Fig. 3a). Furthermore, the substrate was coated with a black matte paint to increase its emissivity, as shown in Fig. 3b. Two distinct tests were conducted for each set of process parameters. The first test focused on measuring the substrate temperatures at points P1 and P2 (see Fig. 3c), with the thermal camera set to a range of $20 - 200$°C. P1 and P2 were selected to check the temperature distribution on the substrate (i.e., plate). The distances were selected to be far from the melting pool and the substrate boundaries, so as not to be

Table 2 Chemical composition of filler wires, and substrate (wt.%)

Materials	C	Mn	Si	P	S	N	Cu	Fe
S235 JR steel	0.19	1.5	–	0.045	0.045	0.014	0.60	Bal
FILCORD C (ER70S-6)	0.08	1.5	0.90	0.025	0.025	–	–	Bal

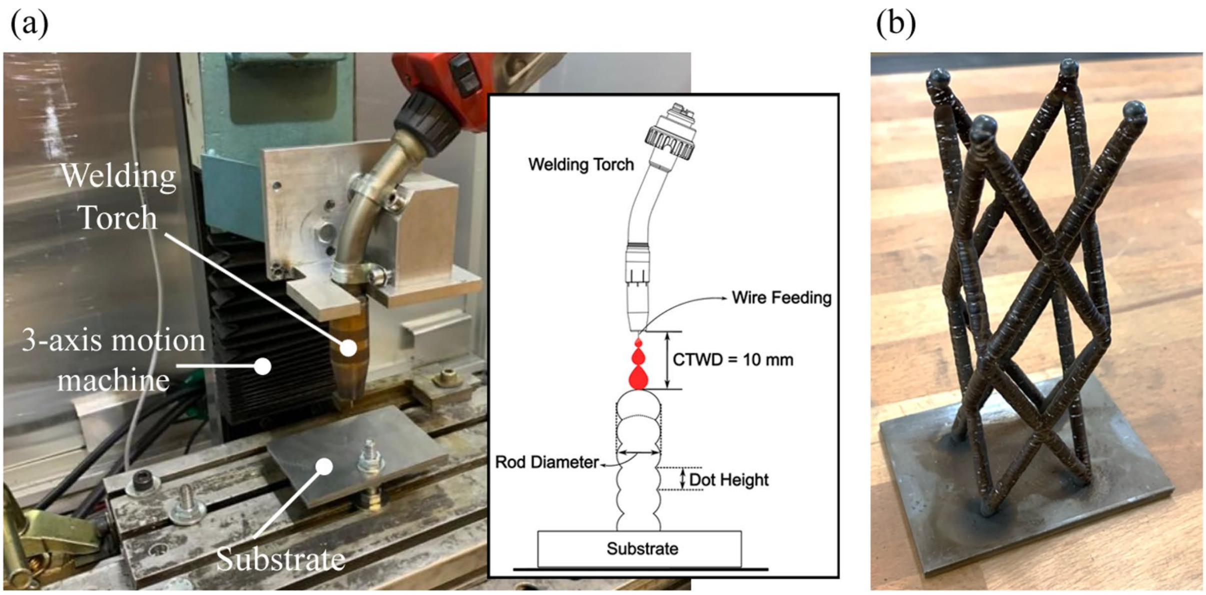

Fig. 2 **a** Experimental system for the DBD-WAAM deposition and **b** example of lattice structure produced by DBD-WAAM

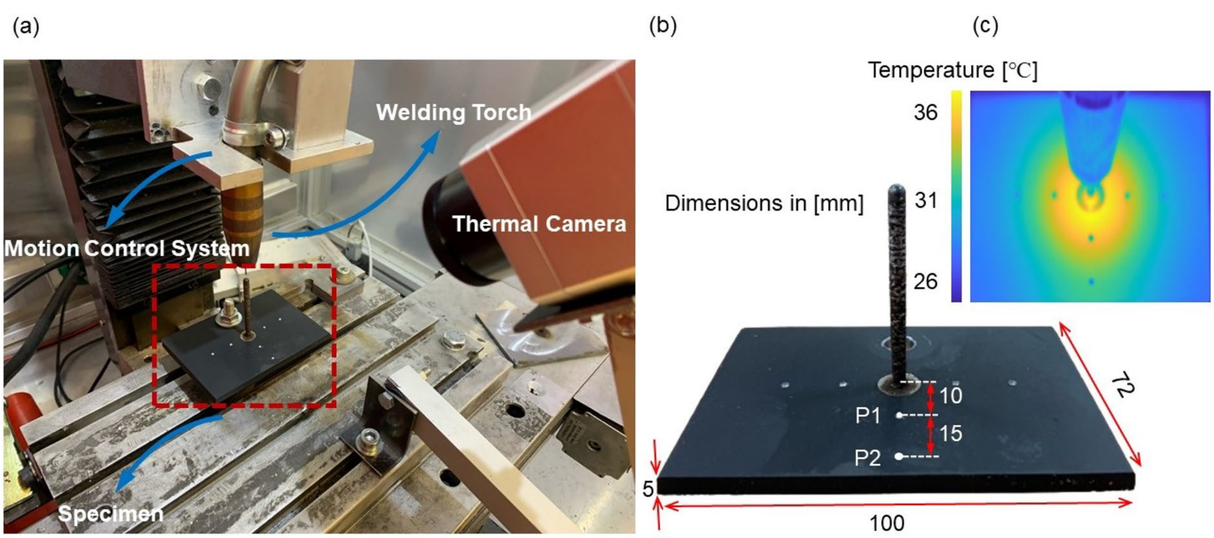

Fig. 3 **a** Experimental setup of DBD WAAM system used in this study to manufacture rods, **b** A sample of manufactured rod via DBD WAAM process, and **c** Temperature distribution recorded by thermal camera

Table 3 Summary of the test series, including the process parameters used, the resulting rod diameter, and average dot height for each case. The wire feed speed (WFS) refers to the nominal value, with the actual speed being slightly lower

ID [−]	WFS [*m/min*]	Arc-on time [*s*]	CTWD [*mm*]	Idle time [*s*]	Energy [*kJ*]	DH [*mm*]	RD [*mm*]
A	4	0.32	10	10	0.3	0.51	4
B	6	0.74	10	20	1.0	1.05	6
C	8	1.15	10	40	2.4	1.45	8

influenced by external effects not modeled in the simulation environment. The substrate was painted to ensure high and constant emissivity, which was calibrated to 0.99 by comparing the results of the thermal camera and the thermocouples on a painted test plate during cooling. The temperature at specific points on the substrate was estimated by post-processing the captured images, where geometric distortion was corrected using prior calibration and image correction algorithms to ensure accurate spatial mapping and temperature distribution.

The second test aimed at measuring the interpass temperature. The thermal camera was set to a range of 200 − 1500°C. Measurements were taken with an emissivity of 1, and the results were post-processed using the actual emissivity values of carbon steel, which vary with temperature, as provided in [38]. The thermal camera recorded the maximum temperature. Subsequently, the interpass temperature (i.e., the temperature prior to the deposition of the next layer) was determined using synchronized start and stop signals, acquired from the welding machine.

For both tests, thermal images were captured using a thermal camera and subsequently post-processed with MathWorks MATLAB. The diameters and heights of all deposited rods were measured, and the average diameter and height were calculated, as summarized in Table 3. To support thermal simulations and microstructural evaluation, additional samples were fabricated using the same process parameters. Multiple dots were deposited on a substrate and sectioned through their centers. The cross-sections were ground and polished according to ASTM E3 standards for metallographic preparation. A 2% Nital solution was used as the etchant [39], and optical microscopy was conducted using a Nikon Eclipse LV150.

For validation of the thermal simulations, the equilibrium phase diagram of a low-carbon steel with a comparable composition was referenced. Key transformation temperatures, including the melting point and the austenite transformation start temperature, were used to identify the melted and heat-affected zones. Based on values reported in the literature [40, 41], the austenite transformation start temperature upon heating was approximated to be 727°C.

3.2 Parameters and inputs for FEM model

During the DBD WAAM process, the step-by-step deposition of droplets induces significant temperature fluctuations within the workpiece. To ensure accurate predictions and a comprehensive understanding of the thermal behavior, temperature-dependent material properties—such as thermal conductivity and specific heat capacity—of low-carbon steel were considered, as reported in [42] (see Table 4). The convection coefficients were determined based on empirical correlations available in the literature [42] and are presented in Table 5. In this table, σ denotes the Stefan–Boltzmann constant, while h_B, h_T, and h_S represent the convection coefficients at the bottom, top, and side surfaces.00

Table 4 Temperature-dependent thermal properties of low carbon steel used in this study for both the deposited part and the base plate [42]

Temperature $[°C]$	Specific Heat $[J/(kg\circ C)]$	Temperature $[\circ C]$	Thermal Conductivity $[W/(m^2\circ C)]$
20	487	20	46
92	487	74	47
116	495	107	47
140	516	215	45
206	530	406	40
235	530	494	38
268	537	594	34
396	550	660	31
377	586	1300	31
652	845	1333	118
747	1352	1399	118
833	626	3000	118
861	595	–	–
3000	595	–	–

Table 5 Heat transfer boundary condition parameters used in this study

Parameter	Value
$h_{B,Substrate}[W/(m^2\ °C)]$	4
$h_{T,Substrate}[W/(m^2\ °C)]$	8.5
$h_{T,Dot}[W/(m^2\ °C)]$	6
$h_{S,All}[W/(m^2\ °C)]$	12
$\epsilon_{T,Substrate}[-]$	1
$\epsilon_{General}[-]$	0.69
$\sigma[W/(m^2\ °C^4)]$	5.67×10^{-8}
$T_{amb}[°C]$	25

Due to the black matte coating applied to the top surface of the substrate during the experimental setup, an emissivity value of 1 was assigned to this surface. In contrast, an emissivity of 0.69 was used for the remaining surfaces. In the final stage of the model setup, the heat source dimensions for each test case—corresponding to rods with different diameters and identified as test IDs A, B, and C in Table 3—were defined based on the geometry of the deposited features. The parameters corresponding to the heat source model (a, b, and c) were set as follows: a and b were assigned values equal to the diameter of the corresponding rod, while c was set equal to the depth of the fusion zone. The parameters are summarized in Table 6. It is worth noting that the power input values listed in Table 6 were calculated by dividing the

Table 6 Heat source dimensions for all rods with different diameters. The power input values listed were calculated by dividing the energy inputs by the corresponding arc-on times provided in Table 3

$RD[mm]$	$P[W]$	$a[mm]$	$b[mm]$	$c[mm]$
4	937.5	3.8	3.8	0.55
6	1351	5.7	5.7	0.83
8	2086	7.22	7.22	1.04

energy inputs by the corresponding arc-on times provided in Table 3.

3.3 Model results and discussion

The validity of the numerical approach presented in this study is confirmed through the analysis of experimental data using two distinct methods: (1) by examining the heat-affected zone derived from optical microscopy images, and (2) by monitoring the temperature evolution during the process using a thermal camera. Initially, the deposition of a single dot on the substrate was simulated for each test case (identified as test IDs A, B, and C in Table 3) using three different heat source models: semi-spherical shape [34], linearly [35], and exponentially decaying [36].

Temperature fluctuations during material deposition significantly influence the resulting microstructure, the HAZ size and shape, and ultimately, the mechanical properties of the material. Thus, accurate representation of the HAZ by heat source models is crucial. In order to validate these models, optical microscopy analysis is essential for comparing the predicted HAZ geometries and boundaries with experimental observations, which are inherently dependent on the deposition parameters.

Figure 4 illustrates the comparison between the models and the actual HAZ found for each parameter condition (A, B and C), each yielding in different dot diameters. The HAZ exhibited essentially a microstructure composed of ferrite with some localized bainite regions. The upper red isotherm, adjacent to the dark-etched zone microstructure (the molten zone of the deposition), delineates the boundary where the melting temperature was reached. Conversely, the lower red isotherm represents the approximate critical temperature derived from the Fe-C phase diagram for the respective chemical composition, i.e., 727°C according to [39, 40]. The locations of these lines are based on microstructural transformations identified through the optical microscopy analysis, illustrating the zone where transformations were identified, representing the peak temperatures and the influence of the welding thermal cycle.

The single dots for the aforementioned test cases were modeled as semi-ellipsoids, with the dimensions provided in Fig. 4. This figure demonstrates that both the semi-spherical and exponentially decaying heat source models exhibit similar behavior regarding the HAZ boundary, showing good agreement between simulation and experimental microstructure. Among these, the semi-spherical model yielded the most accurate results.

In contrast, the linearly decaying heat source model did not accurately predict the HAZ when compared to experimental results. For all models, the worst agreement between simulation and experiment was for the smallest dot (case A

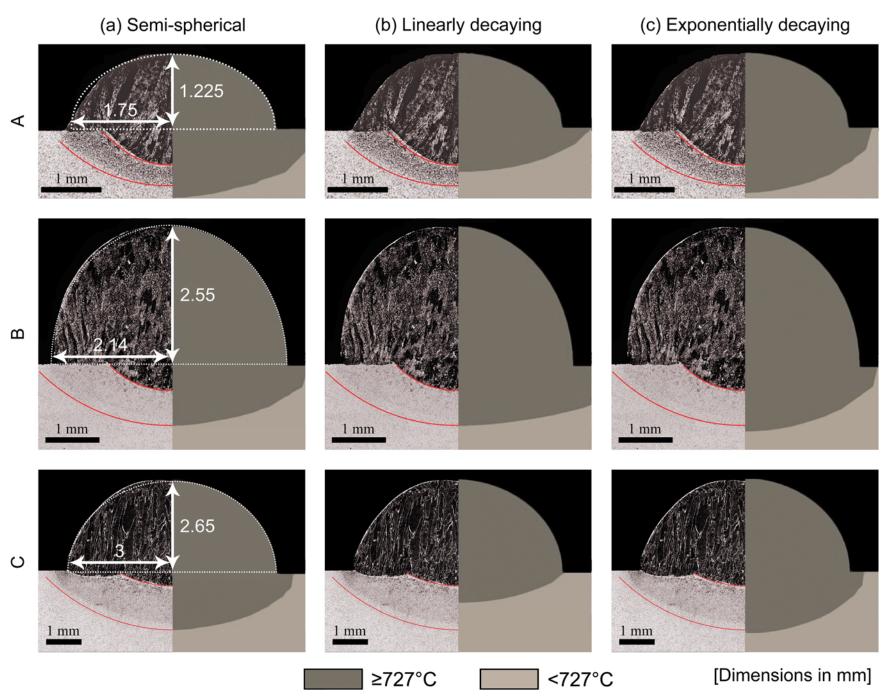

Fig. 4 Comparison of the experimental results and the effect of each model on the HAZ for tests A, B, and C in Table 3). **a** semi-spherical, **b** linearly decaying, and **c** exponentially decaying

in Fig. 4). This smaller dot, resulting from the fastest deposition (0.32 s of arc time), presents a greater challenge for simulation. This is because the deposition process in such fast cases is further from a stable condition, an effect further amplified by the more significant substrate influence on smaller deposited volumes.

For further evaluation, the temperature evolution at two points, $P1$ and $P2$, located 10mm and 25mm from the heat center, was plotted for the three heat source models and compared with the experimental data, as shown in Fig. 5. It can be seen that the temperature at points $P1$ and $P2$ increases during the initial stages of deposition. At this stage, heat is primarily dissipated through conduction from the deposited material into the substrate, resulting in a gradual increase in the substrate's temperature. However, as the deposition progresses and the heat source moves further away from these

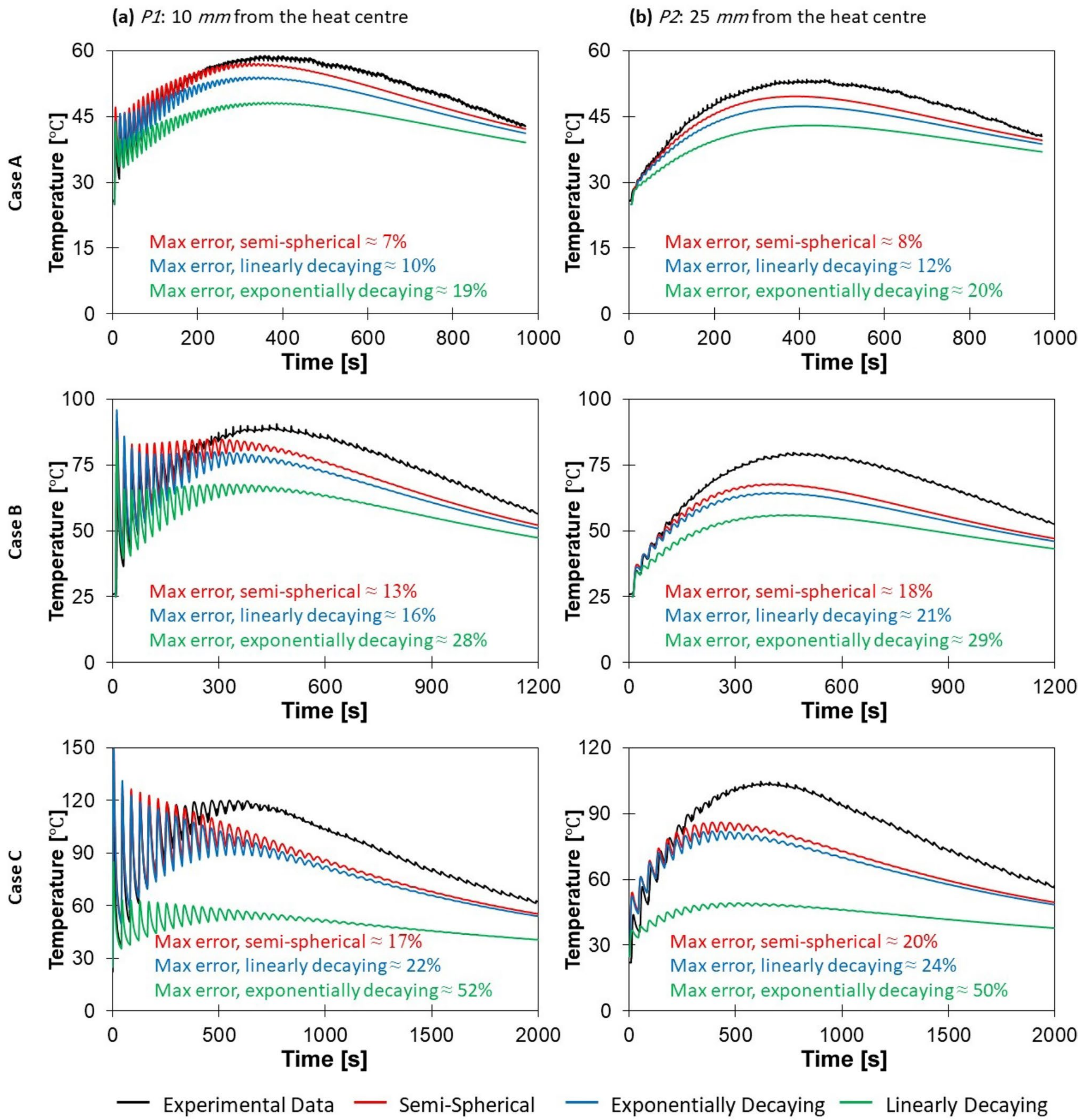

Fig. 5 Comparative analysis of experimental and simulated temperature distributions at distances of **a** 10 mm and **b** 25 mm from the center of the heat source for test cases A, B, and C listed in Table 3

points, convection becomes the dominant mechanism for heat dissipation. Consequently, the heat has less influence on the substrate, and its temperature starts to decrease as it is transferred to the surrounding environment. The figure also shows that the semi-spherical heat source model closely matches the experimental temperature profiles at both $P1$ and $P2$, with minimal error.

Following a detailed analysis of the heat source's influence on the heat-affected zone boundary and temperature evolution, it was concluded that subsequent simulations in this study will utilize the semi-spherical heat source model. In Fig. 6, the interpass temperatures for the three test cases (IDs A, B, and C) are presented. The figure demonstrates good alignment between the numerical predictions and experimental results, both in terms of trends and actual temperature values. A noteworthy observation in Fig. 6 is the stabilization of the interpass temperature after a certain number of dots have been deposited, a trend that is consistently observed in both the experimental and simulation data. Information regarding thermal stabilization is crucial for developing robust welding procedures. This data quantifies the number of discrete depositions (dots) required for the temperature to achieve a stable state. Given that the welding thermal cycle, i.e., the temperature profile and the duration a material is exposed to certain temperatures, can profoundly influence the resulting microstructure, identifying the point at which thermal stabilization occurs provides valuable pratical information.

4 Application of the simulation for interpass temperature: idle time correlation

This section demonstrates the practical application of the developed finite element simulation to establish a quantitative correlation between interpass temperature and the required idle time in the DBD WAAM process. By simulating thermal histories for varying rod diameters and target interpass temperatures, the model provides insights into the thermal behavior of multi-dot builds and the role of process parameters such as heat input idle time. The results are used to generate design curves that assist in process planning and optimization, particularly in determining suitable idle times to maintain desired thermal conditions and avoid heat accumulation.

Figure 7 presents the FEM-predicted idle times required to reach interpass temperatures of 150°C, 200°C, 250°C, and 300°C for rods with diameters of 4 mm, 6 mm, and 8 mm. These correspond to wire feed speeds of 4, 6, and 8 m/min and arc-on times listed in Table 3. At the early stages of deposition, heat dissipates primarily through conduction into the substrate, leading to faster cooling and shorter idle times. However, as the build progresses and the heat-affected area moves further from the substrate, convection becomes the dominant heat dissipation mechanism. This transition results in a quasi-steady thermal state in the system, where the required idle time stabilizes and remains nearly constant, even as the dot number continues to increase. This plateauing behavior is consistently observed across all rod diameters and temperature levels, highlighting the thermal balance between input energy and environmental heat loss.

Additionally, it is observed that for all rods with varying diameters, the required idle time to reach a lower interpass temperature (e.g., 150°C) is higher compared to higher interpass temperatures. This is due to the larger temperature gradient between the hot material and its surroundings at higher temperatures, which drives heat transfer more efficiently and leads to a faster cooling rate. As the material cools and the temperature gradient decreases, the driving force for heat transfer diminishes, slowing the cooling rate and resulting in a longer idle time to reach the target temperature.

Figure 8 presents a design curve for idle time as a function of interpass temperature and rod diameter. This curve, derived from the numerical model, helps determine the

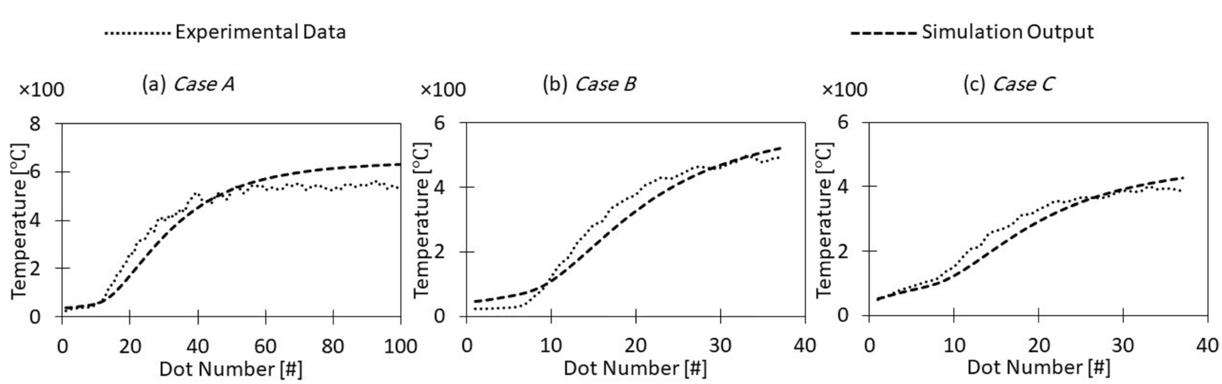

Fig. 6 Quantitative comparison of interpass temperatures between experimental and numerical analyses for three rods with different diameters; **a** *CaseA*, **b** *CaseB*, and **c** *CaseC*

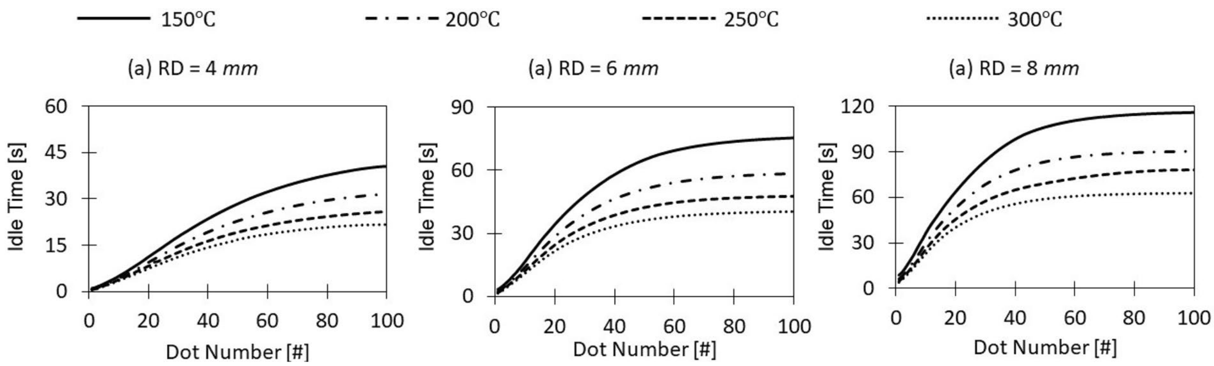

Fig. 7 Quantitative values of the idle time to reach a certain value of interpass temperature during deposition of 100 dots for different rod diameters: **a** $RD = 4mm$, **b** $RD = 6mm$, and **c** $RD = 8mm$

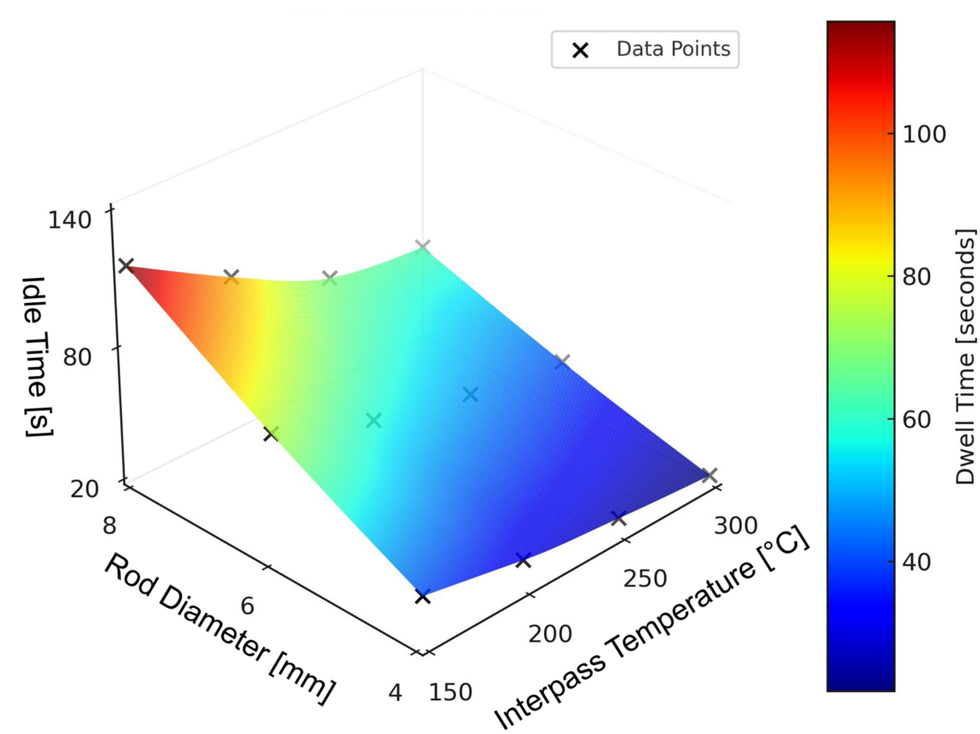

Fig. 8 Design curve illustrating the required interpass idle time as a function of rod diameter and interpass temperature

idle time needed to achieve a desired interpass temperature for a specific rod diameter. As expected, increasing the rod diameter—which requires a higher wire feed speed and heat input—and decreasing the target temperature, both lead to longer idle times. This can be explained by the combined effects of heat input and thermal gradients. A higher WFS parameter deposits more material, increasing heat accumulation within the rod. This extra heat requires more time to dissipate to the surrounding material and environment. Conversely, targeting a lower interpass temperature reduces the temperature difference between the material and its surroundings, hindering heat transfer and necessitating a longer idle time.

The design curve shown in Fig. 8 serves as a practical tool for process designers, enabling them to select appropriate idle times based on the desired interpass temperature and rod diameter. This is particularly valuable in real-time control or automated DBD WAAM systems, where maintaining consistent thermal conditions between dots is essential for build quality and repeatability. Interpass temperature plays a critical role in determining both the geometrical and microstructural characteristics of the deposited material. As shown in recent studies (e.g., [43]), inadequate control of interpass temperature can lead to irregular bead shapes, lack of fusion, grain coarsening, or the accumulation of residual stress. Higher interpass temperatures may result in overmelting of previous dots, leading to smoother fusion but potentially promoting grain growth. On the other hand, lower temperatures can cause insufficient bonding, lack of fusion defects, or uneven dot heights and rod geometry. Therefore, having a predictive model and associated design curves enables improved thermal management, allowing for the optimization of deposition strategies to achieve tailored part properties and enhanced process stability. Furthermore, knowing the interpass temperatures in advance facilitates the development of welding procedures that comply with specific temperature requirements. This is particularly critical in cases where interpass temperature control is necessary to either prevent the precipitation of brittle phases or to avoid rapid cooling and the formation of fragile martensitic microstructures. Depending on the material, adequate temperature control can even prevent the need for additional post-weld heat treatments.

5 Conclusion

The finite element method was employed to simulate the dot-by-dot Wire Arc Additive Manufacturing process of low-carbon steel components. The study aimed to validate the proposed model by comparing the simulated temperature distribution and heat-affected zone with experimental results. Various heat source models, including semi-spherical, linearly decaying, and exponentially decaying models, were tested. The impact of each model on temperature evolution and the heat-affected zone was thoroughly examined. The following conclusions can be drawn from the presented results:

- The semi-spherical heat source model demonstrated superior accuracy in predicting both the heat-affected zone boundary and the temperature evolution. Temperature profiles derived from this model closely aligned with experimental data, exhibiting an average error of approximately 15% in interpass temperature prediction and 20% in substrate temperature prediction in the worst case scenario. This error rate was lower than that observed with the linearly decaying (maximum 24%) and exponentially decaying (maximum 52%) models.
- During the initial stages of deposition, temperature profiles indicate that heat dissipation occurs predominantly through conduction. As the deposition progresses and the heat source translates, convection emerges as the dominant heat dissipation mechanism, consequently leading to a decrease in temperature
- The numerical model accurately predicted the interpass temperatures, with both experimental and simulation data exhibiting a consistent trend. The stabilization of the interpass temperature after a certain number of dots further confirmed the reliability of the proposed model. This provides valuable information in scenarios where interpass temperature control is essential to prevent the precipitation of brittle phases and to mitigate rapid cooling, which can lead to the formation of fragile martensitic microstructures.

One potential development for future studies would be to improve the calibration of simulation parameters, as these are currently tuned based on experimental results. Developing strategies to automate or streamline this calibration process could reduce the computational effort required for model tuning. Additionally, the framework developed in this study could be adapted to simulate the WAAM process for other materials, such as titanium alloys or stainless steel. Integrating the model with multi-physics simulations, including mechanical and microstructural analysis, could provide a more comprehensive understanding of the dot-by-dot WAAM process.

Acknowledgements Part of the research activities were carried out within the CIRCULAR WELD PRIN 2022PNRR project, funded by the European Union—Next Generation EU, Mission 4, Component 1 (CUP: B53D23027320001).

Author contributions Conceptualization: Niccolò Grossi, Gianni Campatelli & Masoud Abbaszadeh; Methodology: Masoud Abbaszadeh, Niccolò Grossi & Gustavo Carvalho; Formal analysis: Masoud Abbaszadeh; Writing—original draft: Masoud Abbaszadeh; Writing—review & editing: Masoud Abbaszadeh, Niccolò Grossi, Gianni Campatelli & Gustavo Carvalho; Project administration: Niccolò Grossi; Funding acquisition: Niccolò Grossi.

Funding Open access funding provided by Università degli Studi di Firenze within the CRUI-CARE Agreement.

Data availability No datasets were generated or analysed during the current study.

Declarations

Conflict of interest The authors declare no Conflict of interest.

References

1. Gonçalves A, Ferreira B, Leite M, Ribeiro I (2023) Environmental and economic sustainability impacts of metal additive manufacturing: a study in the industrial machinery and aeronautical sectors. Sustain Prod Consumption 42:292–308. https://doi.org/10.1016/J.SPC.2023.10.004
2. Brozovsky J, Labonnote N, Vigren O (2024) Digital technologies in architecture, engineering, and construction. Autom Constr 158:105212. https://doi.org/10.1016/J.AUTCON.2023.105212
3. Braun K, Kropp C (2023) Building a better world? competing promises, visions, and imaginaries-in-the-making of the digitalization of architecture and construction. Futures 154:103262. https://doi.org/10.1016/j.futures.2023.103262
4. Carvalho GHSFL, Campatelli G (2023) Deposition strategies using arc oscillation to improve the fabrication of solids by wire arc additive manufacturing. Int J Adv Manuf Technol 128:1559–1576. https://doi.org/10.1007/S00170-023-11912-1/TABLES/9
5. Williams SW, Martina F, Addison AC, Ding J, Pardal G, Colegrove P (2016) Wire + arc additive manufacturing. Mater Sci Technol 32(7):641–647. https://doi.org/10.1179/1743284715Y.0000000073
6. Laghi V, Palermo M, Gasparini G, Trombetti T (2020) Computational design and manufacturing of a half-scaled 3d-printed stainless steel diagrid column. Addit Manuf 36:101505. https://doi.org/10.1016/j.addma.2020.101505
7. Silvestru V-A, Ariza I, Vienne J, Michel L, Aguilar Sanchez AM, Angst U, Rust R, Gramazio F, Kohler M, Taras A (2021) Performance under tensile loading of point-by-point wire and arc additively manufactured steel bars for structural components. Mater Design 205:109740. https://doi.org/10.1016/j.matdes.2021.109740
8. Radel S, Diourte A, Soulié F, Company O, Bordreuil C (2019) Skeleton arc additive manufacturing with closed loop control. Addit Manuf 26:106–116. https://doi.org/10.1016/j.addma.2019.01.003
9. Singh CP, Sarma R, Rajput AS, Kapil S (2024) A nature-inspired build strategy for consistently fabricating intricate objects by wire-arc-based directed energy deposition. Progress in Additive Manufacturing, 1–21 https://doi.org/10.1007/S40964-024-00909-1
10. Arrè L, Laghi V, Palermo M, Gasparini G, Trombetti T (2023) Wire-and-arc additive manufacturing for lattice steel structures: overview of the experimental characterization on dot-by-dot rods. Ce/papers 6(3–4):757–762
11. Yu Z, Ding D, Pan Z, Li H, Lu Q, Fang X (2021) A strut-based process planning method for wire arc additive manufacturing of lattice structures. J Manuf Process 65:283–298. https://doi.org/10.1016/j.jmapro.2021.03.038
12. Arrè L, Laghi V, Palermo M, Gasparini G, Trombetti T (2023) Wire-and-arc additive manufacturing for lattice steel structures: overview of the experimental characterization on dot-by-dot rods. ce/papers 6:757–762. https://doi.org/10.1002/CEPA.2622
13. Lettori J, Esposto C, Peruzzini M, Pellicciari M, Raffaeli R (2025) Geometrical characterization of circular multi-layered cmt waam specimens by 3d structured light scanning. Int J Adv Manuf Technol 136:5305–5334. https://doi.org/10.1007/S00170-025-15107-8
14. Liu M, Yang Y, Song C, Liu Z, Li Y, Zhang S (2025) Effect of cmt-cs additive manufacturing on the surface quality, microstructure and properties of 316l stainless steel. Int J Adv Manuf Technol 138:5467–5482. https://doi.org/10.1007/S00170-025-15825-Z
15. Mechtcherine V, Grafe J, Nerella VN, Spaniol E, Hertel M, Füssel U (2018) 3d-printed steel reinforcement for digital concrete construction—manufacture, mechanical properties and bond behaviour. Constr Build Mater 179:125–137. https://doi.org/10.1016/j.conbuildmat.2018.05.202
16. Grossi N, Lazzeri F, Venturini G (2025) Deposition strategies for bar intersections using dot-by-dot wire and arc additive manufacturing. J Manuf Mater Process 9:77. https://doi.org/10.3390/jmmp9030077
17. Classen M, Ungermann J, Sharma R (2020) Additive manufacturing of reinforced concrete-development of a 3d printing technology for cementitious composites with metallic reinforcement. Appl Sci 10(10):3791. https://doi.org/10.3390/APP10113791
18. Müller J, Grabowski M, Müller C, Hensel J, Unglaub J, Thiele K, Kloft H, Dilger K (2019) Design and parameter identification of wire and arc additively manufactured (waam) steel bars for use in construction. Metals **9**(7)https://doi.org/10.3390/met9070725
19. Abe T, Sasahara H (2019) Layer geometry control for the fabrication of lattice structures by wire and arc additive manufacturing. Addit Manuf 28:639–648. https://doi.org/10.1016/j.addma.2019.06.010
20. Heimig T, Kerber E, Stumm S, Mann S, Reisgen U, Brell-Cokcan S (2020) Towards robotic steel construction through adaptive incremental point welding. Construct Robot 4(1):49–60. https://doi.org/10.1007/s41693-019-00026-4
21. Mao H, Liu C, Ling X, Xu H, Xie J, Fu R, Jing C, Wang D, Wang C, Lv J (2025) Effects of arc waveforms on morphology, microstructure, and properties of unsupported bars in wire and arc additive manufacturing. J Mater Process Technol 337:118722. https://doi.org/10.1016/J.JMATPROTEC.2025.118722
22. Hergul Y, Goynuk T, Yucel M, Can G, Yaman U (2025) Performance and microstructure analysis of cylindrical rods fabricated by dot-by-dot waam for aerospace applications. Progress in Additive Manufacturing, 1–16 https://doi.org/10.1007/S40964-025-01166-6
23. Laghi V, Arrè L, Gasparini G, Trombetti T, Palermo M (2025) Design strength parameters of dot-by-dot wire-and-arc additively manufactured stainless steel bars. Structures 71:107857. https://doi.org/10.1016/j.istruc.2024.107857
24. Barath Kumar MD, Manikandan M (2022) Assessment of process, parameters, residual stress mitigation, post treatments and finite element analysis simulations of wire arc additive manufacturing technique. Met Mater Int 28(1):54–111. https://doi.org/10.1007/s12540-021-01015-5
25. Chergui A, Villeneuve F, Béraud N, Vignat F (2022) Thermal simulation of wire arc additive manufacturing: a new material deposition and heat input modelling. Int J Interactive Design Manuf (IJIDeM) 16(1):227–237. https://doi.org/10.1007/s12008-021-00824-7
26. Montevecchi F, Venturini G, Grossi N, Scippa A, Campatelli G (2018) Idle time selection for wire-arc additive manufacturing: a finite element-based technique. Addit Manuf 21:479–486. https://doi.org/10.1016/j.addma.2018.01.007
27. Amal MS, Justus Panicker CT, Senthilkumar V (2022) Simulation of wire arc additive manufacturing to find out the optimal path planning strategy. Materials Today Proceedings 66:2405–2410. https://doi.org/10.1016/j.matpr.2022.06.338. 2022 International Conference on Recent Advances in Engineering Materials
28. Ding J, Colegrove P, Mehnen J, Williams S, Wang F, Almeida PS (2014) A computationally efficient finite element model of wire and arc additive manufacture. Int J Adv Manuf Technol 70(1):227–236. https://doi.org/10.1007/s00170-013-5261-x
29. Wu B, Pan Z, Ziping Y, Duin S, Li H, Pierson E (2021) Robotic skeleton arc additive manufacturing of aluminium alloy. Int J Adv Manuf Technol 114(9):2945–2959. https://doi.org/10.1007/s00170-021-07077-4
30. Sampaio RFV, Pragana JPM, Bragança IMF, Silva CMA, Nielsen CV, Martins PAF (2023) Modelling of wire-arc additive

manufacturing—a review. Adv Ind Manuf Eng 6:100121. https://doi.org/10.1016/j.aime.2023.100121
31. Tröger J-A, Hartmann S, Treutler K, Potschka A, Wesling V (2025) Simulation-based process parameter optimization for wire arc additive manufacturing. Progress Additive Manuf 10:1–14. https://doi.org/10.1007/s40964-024-00597-x
32. Jayanath S, Achuthan A (2018) A computationally efficient finite element framework to simulate additive manufacturing processes. J Manuf Sci Eng 140(4):041009. https://doi.org/10.1115/1.4039092
33. Goldak J, Chakravarti A, Bibby M (1984) A new finite element model for welding heat sources. Metall Trans B 15(2):299–305. https://doi.org/10.1007/BF02667333
34. Bruna-Rosso C, Demir AG, Previtali B (2018) Selective laser melting finite element modeling: validation with high-speed imaging and lack of fusion defects prediction. Mater Design 156:143–153. https://doi.org/10.1016/j.matdes.2018.06.037
35. Ladani L, Romano J, Brindley W, Burlatsky S (2017) Effective liquid conductivity for improved simulation of thermal transport in laser beam melting powder bed technology. Addit Manuf 14:13–23. https://doi.org/10.1016/j.addma.2016.12.004
36. Liu S, Zhu H, Peng G, Yin J, Zeng X (2018) Microstructure prediction of selective laser melting alsi10mg using finite element analysis. Mater Design 142:319–328. https://doi.org/10.1016/j.matdes.2018.01.022
37. Huang H, Ma N, Chen J, Feng Z, Murakawa H (2020) Toward large-scale simulation of residual stress and distortion in wire and arc additive manufacturing. Addit Manuf 34:101248. https://doi.org/10.1016/j.addma.2020.101248
38. Sadiq H, Wong MB, Tashan J, Al-Mahaidi R, Zhao X-L (2013) Determination of steel emissivity for the temperature prediction of structural steel members in fire. J Mater Civ Eng 25(2):167–173. https://doi.org/10.1061/(ASCE)MT.1943-5533.0000607
39. Voort GFV (ed) (2004) ASM Handbook Volume 9: Metallography and Microstructures. ASM Handbook, vol. 9. ASM International, Materials Park, OH
40. Villars P, Okamoto H (eds) (2016) ASM Handbook Volume 3: Alloy Phase Diagrams. ASM Handbook, vol. 3. ASM International, Materials Park, OH
41. Massalski TB, Okamoto H, Subramanian PR, Kacprzak L (eds) (1990) Binary Alloy Phase Diagrams, 2nd edn. ASM International, Materials Park, OH. Product code: 57718G
42. Alto P (ed) (2007) Carbon Steel Handbook. EPRI Project Manager, Hillview Avenue, Palo Alto, California, USA
43. Teixeira FR, Scotti FM, Jorge VL, Scotti A (2023) Combined effect of the interlayer temperature with travel speed on features of thin wall waam under two cooling approaches. Int J Adv Manuf Technol 126:273–289. https://doi.org/10.1007/S00170-023-11105-W